



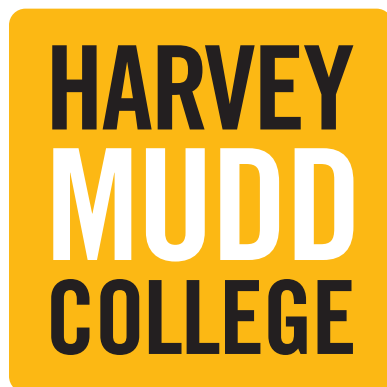
DEM Inversion Failures During Solar Flares

Lucien Mallett

P.S. Athiray ¹, Advisor
Amy Winebarger ², Advisor

Ann Esin, HMC Advisor

May, 2024



Harvey Mudd College
Department of Physics

¹ University of Alabama, Huntsville

² University of Alabama, Huntsville and NASA Marshall Space Flight Center

Copyright © 2024 Lucien Mallett.

The author grants Harvey Mudd College the nonexclusive right to make this work available for noncommercial, educational purposes, provided that this copyright statement appears on the reproduced materials and notice is given that the copying is by permission of the author. To disseminate otherwise or to republish requires written permission from the author.

Acknowledgements

Over the summer, this work was supported in part by NSF award #1950831.

I am deeply grateful to Amy and Athiray, who began this work with me in the summer of 2023. They introduced me to a field of study that I fell in love with, and have changed the course of my life.

Harvey Mudd College is a special place, and it is because of the people. My professors have always pushed me to be the best version of myself that I can be, and I am forever grateful for their eternal support. I would not be here without them. Professors Esin, Shuve, Yong, Tamayo, and Dodds are among the many that have helped me along the way; my professors are uniquely talented in making me feel excited about the material I have learned.

My peers, too, deserve recognition. My friends have been there for me throughout my time at Mudd, and have helped me grow: Lucia M., Kai R., Emilynne N., Saheli P., and Avery P. were some of the first people I ever met at Mudd, and I owe my success to their enthusiasm and care.

I would also like to extend a special dedication to my cats, Penny (who sadly did not make it to this year) and Sarah. My first year at Harvey Mudd College was online, and having them purring on my lap alleviated a not-insignificant portion of the hardship.

Abstract

Large eruptive solar flares can rapidly heat plasma to temperatures on the order of 10^6 K, producing bright emission in the extreme ultraviolet (EUV) and X-ray range. By applying differential emission measure (DEM) inversion methods to narrow-band EUV images, such as those taken by the Atmospheric Imaging Assembly aboard the Solar Dynamics Observatory, it is typically possible to characterize the thermal distribution of plasma in the solar atmosphere with high spatial and temporal resolution. However, during observations of solar flares, it becomes challenging or impossible to determine DEM solutions for all pixels and during all time frames. There are several potential reasons for this: for example, the sudden brightness of these events results in several instrumental artifacts; additionally, plasma in solar flares occurs at a wide range of temperatures and is expected to depart from thermal and/or ionization equilibrium.

In this thesis, I present results from the DEM analysis of two X-class solar flares. I remove instrumental artifacts, demonstrate that DEM inversion failure is strongly localized to the tops of coronal loops in post-flare times, and suggest further avenues of inquiry using non-equilibrium response functions.

Contents

1	The Sun	4
1.1	The Sun	4
1.2	Solar Flares	6
2	Spectral Diagnostics: Instruments and Analytical Tools	10
2.1	The Atmospheric Imaging Array	11
2.1.1	Plate Scale and Spatial Resolution	11
2.1.2	Saturation and Temporal Resolution	11
2.1.3	Response Functions and Sensitivities	13
2.2	DEM Inversion	16
2.2.1	Differential Emission Measure	16
2.2.2	DEM Inversion	17
2.2.3	Sparse DEM Inversion	17
3	Data	19
3.1	Data Collection	19
3.2	Data Processing	19
4	Analysis of Inversion Failures	24
4.1	Saturation	24
4.2	Status Codes	24
4.3	Spatial Locations	28
4.4	Loci Plots	30
4.5	Conclusions and Further Study	32

List of Figures

1.1	The Sun's layers and their associated temperatures	5
1.2	The solar corona and chromosphere during a solar eclipse	5
1.3	Temperature vs. radius in the solar atmosphere	6
1.4	Diagram of magnetic reconnection causing a solar flare, with example image	7
1.5	Typical emission schematic during flare phases	9
2.1	Example AIA images in EUV channels	12
2.2	AIA effective areas as a function of wavelength for EUV channels . .	14
2.3	AIA temperature response functions	15
2.4	Example of EM curve output	18
3.1	GOES X-Ray curves for flares under examination	20
3.2	AR 11263 in 6 EUV channels	22
3.3	AR 12158 in 6 EUV channels	23
4.1	Cumulative emission measure stills for both flares under study . .	25
4.2	Sample of status code outputs for both flares under study	27
4.3	Standard model of a solar flare	29
4.4	Loci plots at different locations	31

List of Tables

1.1 Flare classifications by GOES X-Ray observations	8
2.1 Dominant emission lines and temperatures in AIA EUV channels during solar flares	13

Chapter 1

The Sun

1.1 The Sun

The Sun is a medium-sized star, located at the center of our solar system. It is primarily composed of hydrogen and helium, with some trace amounts of heavier elements, ionized into a hot sphere of plasma.

Solar physicists divide the Sun into several layers, as shown in Figure 1.1, based on similar properties such as temperature and density. The hottest and densest region of the Sun is its core, where nuclear fusion takes place at a temperature of roughly 15 MK. Energy propagates outwards from these reactions through the **convective and radiative layers** of the Sun, and the plasma becomes cooler and cooler as distance increases from the source of energy. The lowest layer of the Sun's atmosphere, the **photosphere**, is what we perceive on Earth as the disk or "surface" of the Sun, as most of the photons we observe are emitted from this thin layer. The photosphere is defined roughly as the region where the optical depth of the plasma decreases to unity for 5000 Å, at which point the mean free path of the photons is long enough for them to escape the Sun entirely. The temperature here is roughly 5700 K.

At the upper edge of the photosphere, the temperature reaches a minimum value of about 4400 K, and then, counterintuitively, begins to rise again. This region of slow increase, which extends up until the temperature has increased to \sim 20000 K, is called the **chromosphere**. After this point, a far more dramatic change in temperature occurs in the so-called **transition region**, a stretch of the solar atmosphere where the temperature abruptly spikes to around \sim 10⁵ K [1].

Following the transition region, farther out still from the Sun's surface — most easily visible during solar eclipses, as in Figure 1.2 — is the **solar corona**. Despite extending millions of kilometers into outer space, it reaches temperatures more akin to those in the core: \sim 10⁶ K (see Figure 1.3).

These extreme atmospheric temperatures have baffled researchers for decades, and the **coronal heating problem** is, as yet, an outstanding problem in solar

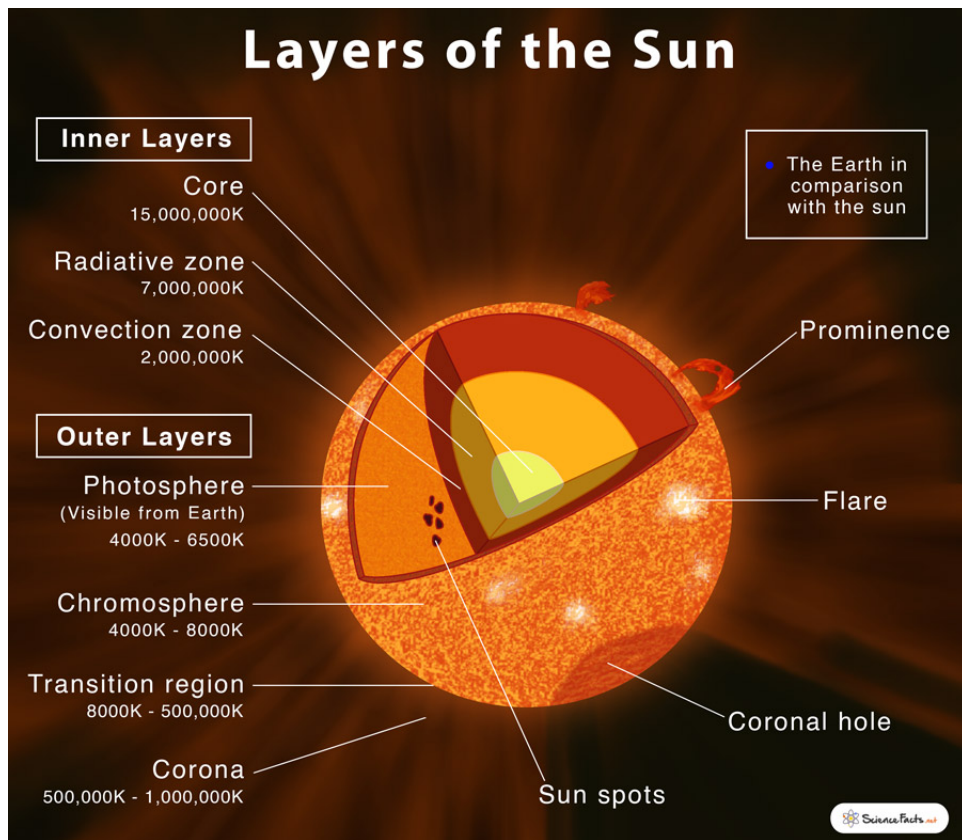


Figure 1.1: A diagram of the Sun's layers, and associated temperatures. From [2].

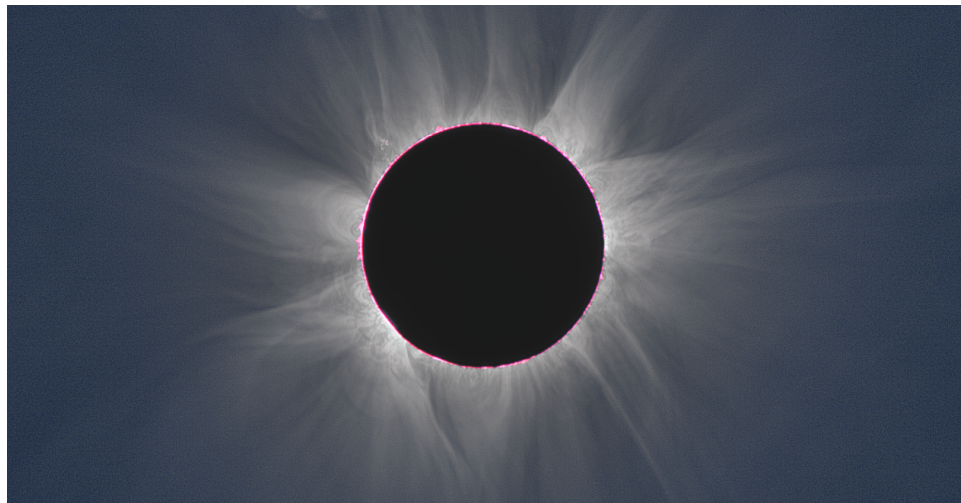
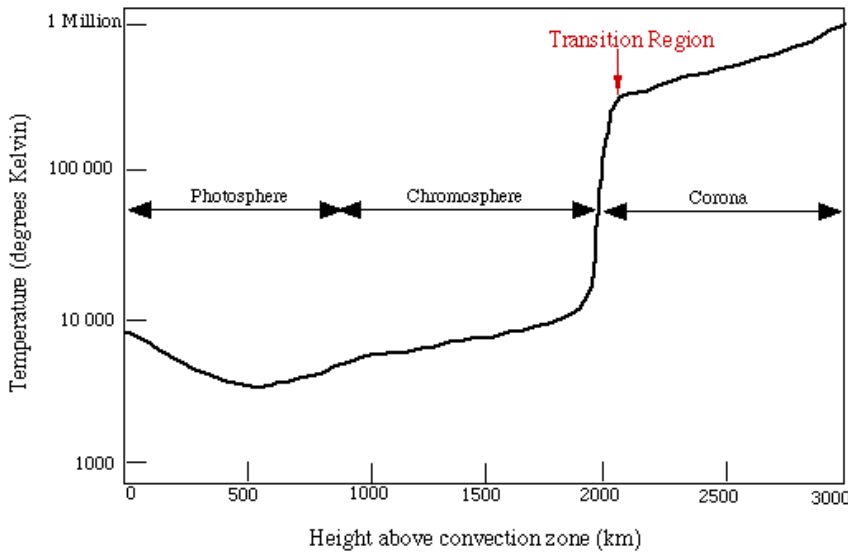


Figure 1.2: The solar corona, visible during a solar eclipse in 2013. Around the edge of the Moon, the reddish chromosphere is also slightly visible. From [3].



(a)

Figure 1.3: A graph of the temperatures measured in the solar atmosphere as a function of height above the convection zone (the outermost layers of the solar interior). From [4].

physics. A key factor in the solution is almost certainly the **solar dynamo** and solar magnetic field. The solar dynamo is the process by which the Sun's differential rotation and convection churns the solar plasma and generates a strong magnetic field in and around the star, extending far into outer space.

Plasma in the Sun flows at the whim of gravity, differential rotation, convection, and the Coriolis force, among other influences. Since plasma is comprised of ions, this motion of charged particles produces a strong magnetic field, anchored in the solar convection zone and extending beyond the photospheric surface and into the corona. This magnetic field can be thought of as a complex assortment of loops extending through the surface of the Sun and interacting with the moving plasma. The interaction of electrically conductive and magnetized plasma with this field is the cause of many interesting features visible in the Sun's atmosphere, such as those in so-called **active regions**, locations of high magnetic activity on the Sun's surface.

1.2 Solar Flares

Sometimes, in active regions, magnetic field lines rearrange and reconnect as the plasma moves. A visual example of this is diagrammed in Figure 1.4.

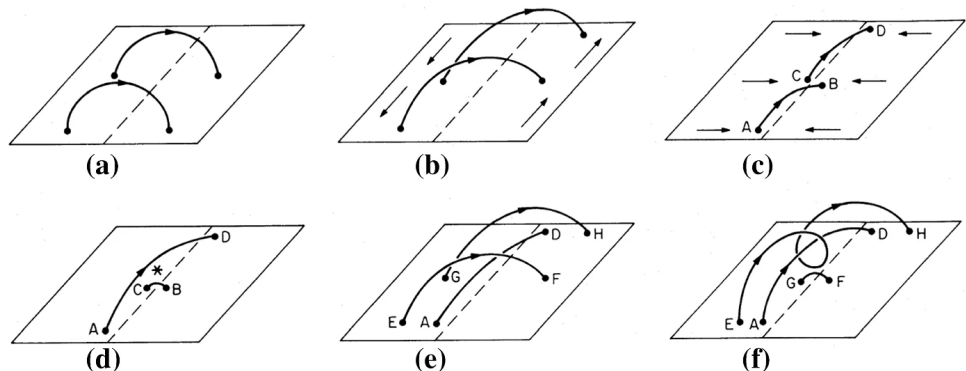
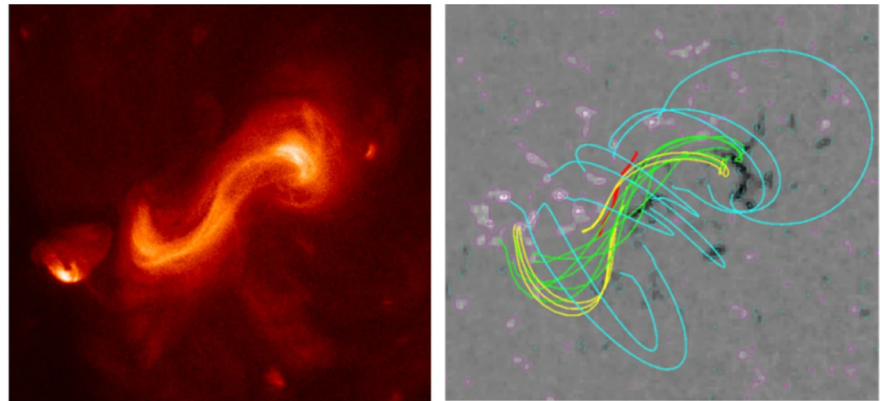


Figure 1.4: Adapted from [5]. **Top left:** an image of an active region on the Sun in X-rays. **Top right:** Colored lines model the magnetic field lines present in this active region, where the blue lines arch over the green, red, and yellow field lines. These lines are overlaid on a line-of-sight magnetogram, where white indicates magnetic field lines coming out of the page and black indicates field lines going in. **Bottom:** A diagram indicating how the flare may have developed. In panels (a-c), the plasma is sheared and pushed together. Between panel (c) and (d), the magnetic field lines break and reconnect. In panels (e-f), overarching field lines that did not break interact with the newly reconnected field.

This magnetic reconnection liberates energy in the form of heat, rapidly altering the characteristics of the surrounding plasma. The temperatures and densities rise significantly, electron distributions may become non-Maxwellian, and plasma is accelerated. This is called a **solar flare**. Plasma in solar flares produces bright emission in infrared, UV-visible, extreme ultraviolet (EUV), and soft X-ray (SXR) regions of the electromagnetic spectrum.

Solar flares occur over the course of seconds to hours, and when observed, their evolutions are divided into three stages: the pre-flare/onset phase, where the event is triggered (characterized by a slow increase in SXR flux); the impulsive phase (characterized by a sharp increase in SXR flux); and the gradual phase (during which the SXR flux decays) [1]. A rough schematic of expected fluxes in various parts of the electromagnetic spectrum can be seen in Figure 1.5.

Flares are typically classified by their peak flux in the 1.0 Å–8.0 Å band (see Table 1.1), as measured by Geostationary Operational Environmental Satellite (GOES), a set of geosynchronous weather satellites. For example, a flare that has a peak flux of $5.5 \times 10^{-6} \text{ W/m}^2$ would be classified as a C5.5 flare. In this thesis, we examine two X-class solar flares.

Class	Flux [W/m ²]
A	$<10^{-7}$
B	$10^{-7}\text{--}10^{-6}$
C	$10^{-6}\text{--}10^{-5}$
M	$10^{-5}\text{--}10^{-4}$
X	$>10^{-4}$

Table 1.1: Flare classifications. Flux is measured in the 1.0 Å–8.0 Å band by Geostationary Operational Environmental Satellite (GOES).

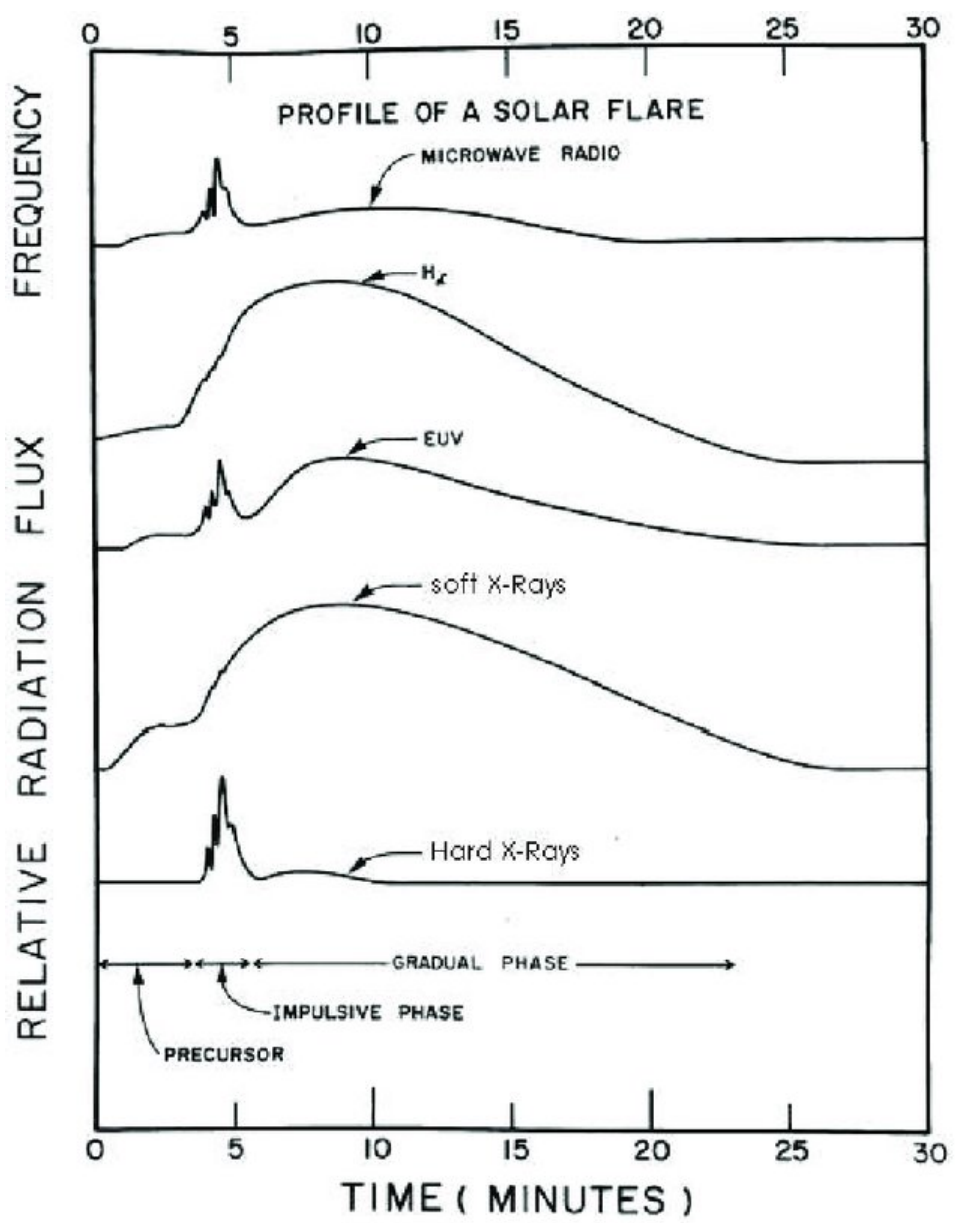


Figure 1.5: Typical flare phases as presented by [6] in multiple different regions of the electromagnetic spectrum. Every flare is different, and these timescales and fluxes vary.

Chapter 2

Spectral Diagnostics: Instruments and Analytical Tools

To develop our understanding of the physics governing solar flares, it is important for us to understand the distribution of plasma temperatures present in them. Since solar flares are local phenomena — both spatially and temporally — on the surface of the Sun, it is especially important that we can distinguish between plasma at different locations and during specific times. However, this is not a trivial measurement: unlike materials on Earth, we cannot know the temperature of plasma in the Sun by measuring it directly.

In lieu of a Sun-proof thermometer, we can use an alternate method: spectral diagnostics. A material's temperature determines its black-body radiation; additionally, it changes the proportions of ionization states present, which affect the relative strengths of ionization lines. This means that materials emit light in a spectrum that is, to a large degree, temperature-dependent.

As described later in this chapter, when we observe a plasma's emission with prior knowledge about its elemental abundances, it is typically possible to reconstruct the amount of emission that came from plasma of any given temperature along the line-of-sight. Therefore, to determine temperatures of features on the Sun, the data for this project ought to consist of images of the Sun, taken in several narrow wavelength bands. The relative intensities of light in different bands in any given pixel should be enough to derive the temperature of plasma along that pixel's line-of-sight.

Fortunately, thanks to the efforts of the space program, such data is readily available. For this project, we made use of data taken by the Atmospheric Imaging Array.

2.1 The Atmospheric Imaging Array

The Atmospheric Imaging Array (AIA) is an instrument onboard the Solar Dynamics Observatory (SDO) satellite. It consists of four telescopes with primary mirror diameters of 20 cm, and each telescope images using a $4096 \text{ px} \times 4096 \text{ px}$ charge-coupled device (CCD) camera. It collects images of the full solar disk in 10 narrow-band channels: 3 in the UV-visible range and 7 in the extreme ultraviolet (EUV) range. In each channel, images are returned as 4096×4096 arrays where values take on a unit of “data number (DN)” in each pixel. The instrument provides high-quality data that is well-suited for performing spectral diagnostics of the solar atmosphere. Example AIA images for the channels we used in this project can be found in Figure 2.1.

2.1.1 Plate Scale and Spatial Resolution

The AIA has an effective focal length of 4.125 m and a pixel size of $12 \mu\text{m}$ [8]. This means that the angular size of the pixel, or plate scale, is

$$\frac{\text{angular separation}}{\text{focal length}} \times \text{pixel size} = \text{angular size of the pixel}$$
$$\frac{1 \text{ rad}}{4.125 \text{ m}} \times 12 \mu\text{m} = 0.6''/\text{px}.$$

which defines how much of the sky a single pixel ‘views’. Since EUV wavelengths are so small, the spatial resolution of AIA for EUV channels is dominated by effects other than Rayleigh criterion (i.e., diffraction), such as errors in the telescope’s alignment or assembly, telescope jitter, and charge spreading on the camera. Cumulatively, when errors are added in quadrature, AIA channels in the extreme ultraviolet wavelengths have an expected resolution of approximately $1.5''$ – $1.75''$ [8].¹ In other words, AIA can resolve two point sources as long as their angular separation is greater than this value, which, due to the distance between AIA and the Sun, corresponds roughly to 1100 km when observing the solar disk [9].

2.1.2 Saturation and Temporal Resolution

The Atmospheric Imaging Array produces images via charge-coupled devices (CCDs). These detectors absorb incoming photons at each pixel and accumulate charge in an electron potential well. The CCDs report a value (a data number DN) that reflects the number of electrons accumulated in each pixel.

When observing bright emission such as the emission from solar flares, these devices can become oversaturated and data to become of poor quality. This can

¹ Some sources instead report the Nyquist limit of $1.2''$. Since resolution in pixels is inherently discrete, both imply that sources may be distinguished when they are separate pixels.

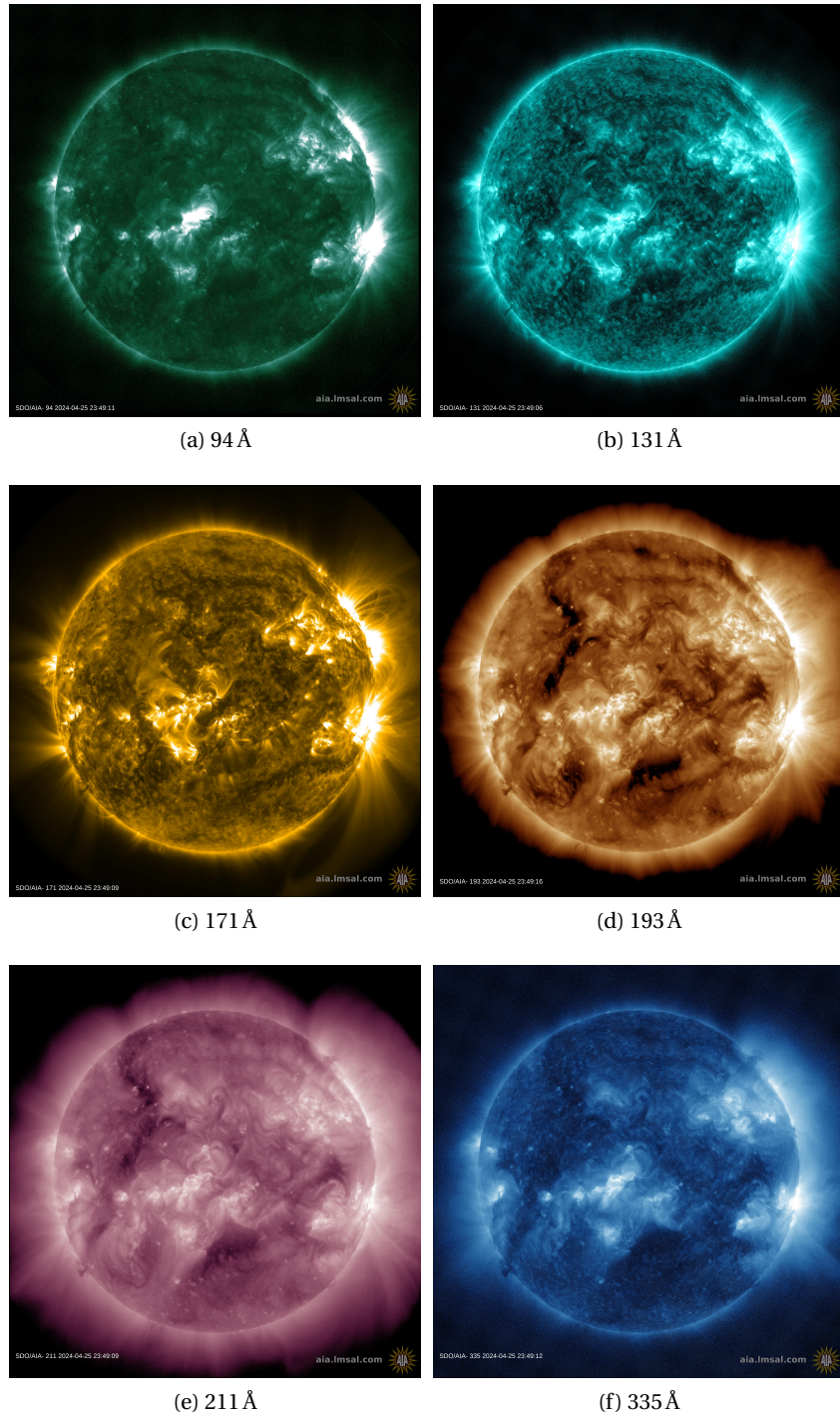


Figure 2.1: Example AIA images taken on April 25, 2024. Retrieved from [7].

happen due to the potential well being unable to collect more charge (primary saturation), which then may cause charge to spill over into nearby pixels (blooming). For the Atmospheric Imaging Array, it is common in the literature to assume that a pixel intensity value of $\geq 15\,000$ DN is saturated [10].

Temporally, AIA collects eight full images roughly every 12 s, where each telescope images in two different channels. The exposure of each image is controlled with an automatic exposure control algorithm. Typically, images are captured using a standard exposure time; during periods of bright emission, AIA reduces exposure times to avoid saturated pixels [8].

2.1.3 Response Functions and Sensitivities

Six of AIA's EUV channels are sensitive to plasma in the solar atmosphere, since these channels correspond primarily to optically-thin radiation from the transition region and solar corona [1, see section 2.4.4]. These channels are therefore particularly useful for studying solar flares, which occur in these layers. Effective-area functions, indicating the instrument's wavelength passbands, can be seen in Figure 2.2.

Several emission lines contribute to the intensity measured in any channel. In solar flares, however, these channels are primarily dominated by emission lines from iron which has been highly ionized. Since iron has many complex transitions, its emission provides excellent diagnostics for characterizing plasma density, temperature, and velocity. Each channel is primarily useful for measuring plasma at certain temperatures, as shown in Table 2.1.

Filter Å	Ions	$\log(T)$
94	Fe XX, XVIII	7.0, 6.85
131	Fe XXIII, XXI	7.15, 7.05
171	Fe IX	5.85
193	Fe XXIV	7.25
211	Fe XVII, XIV	6.6, 6.3
335	Fe XVI	6.45

Table 2.1: Dominant emission lines and associated temperatures *during solar flares*, adapted from [11].

Based on information like that shown in table 2.1, the **temperature response function** of an AIA channel i , $K_i(T)$, represents the instrument's sensitivity to detecting plasma at temperature T . It gives the expected photon flux per pixel on the detector due to an emitting isothermal plasma, and is calculated by combining the plasma's known or predicted spectrum with the instrument's wavelength response [12, see section 2.5].

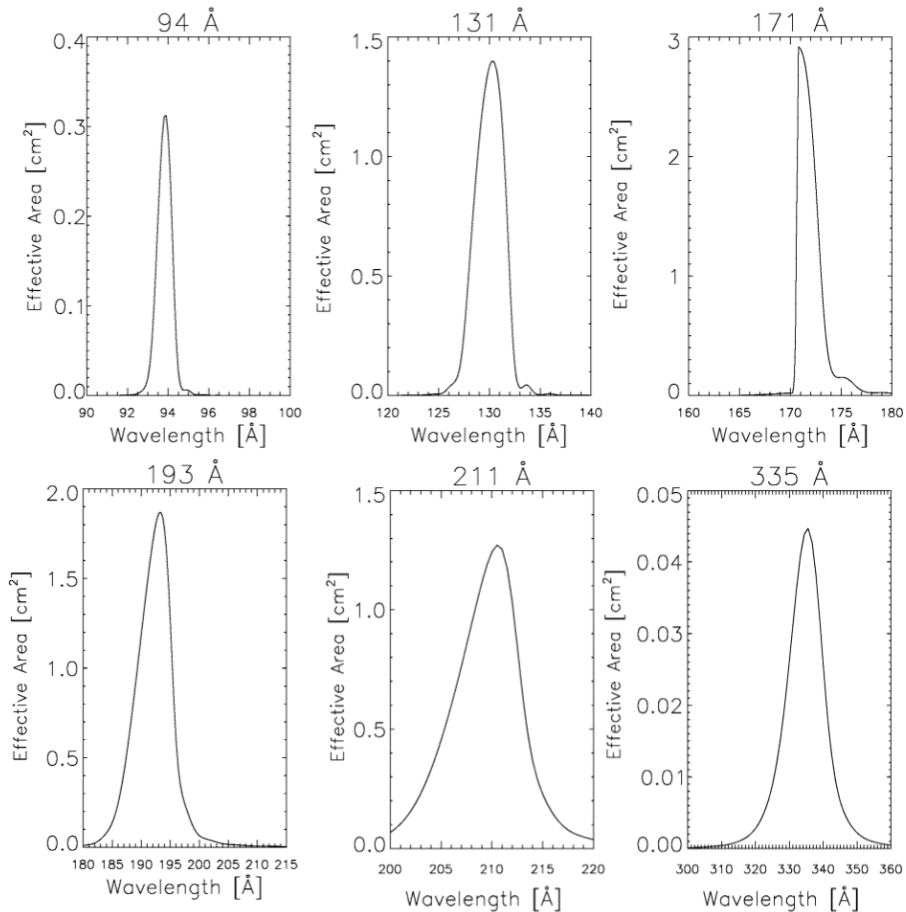


Figure 2.2: AIA effective areas for EUV channels as a function of wavelength, demonstrating the passband of each channel. The channels have varying widths. From [12].

For this project, we used the standard `aia_get_response.pro` code from SolarSoftware to generate the temperature response functions for the AIA channels with flags `timedepend_date` and `eve_norm`, with CHIANTI database vers. 10.0.2 [13]. The generated response functions assume accepted coronal abundances [14], ionization equilibrium, and a Maxwellian electron distribution. They can be seen in Figure 2.3.

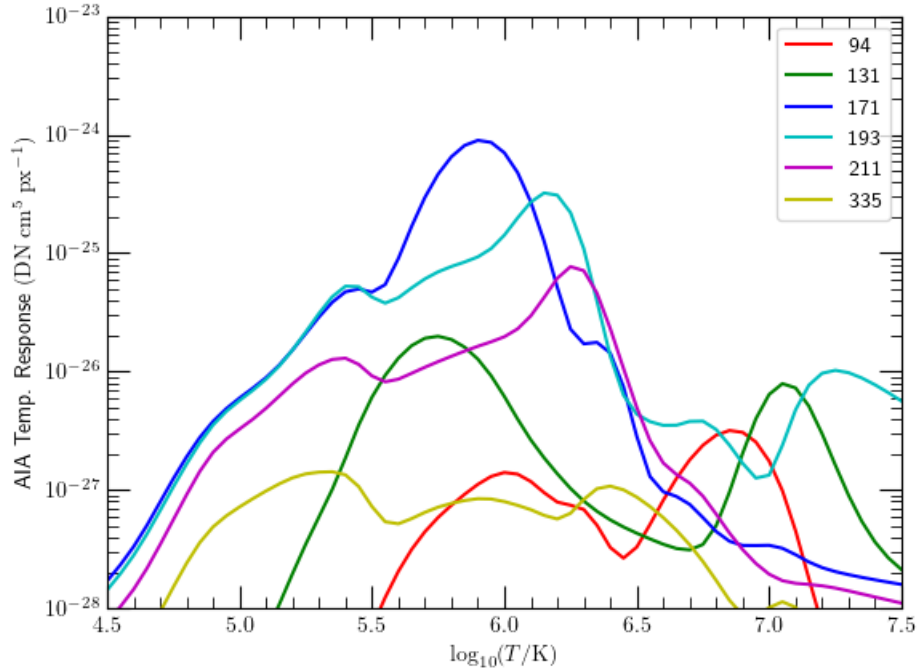


Figure 2.3: Temperature response functions K_i for AIA, as calculated by `aia_get_response.pro` from SolarSoft and CHIANTI v.10.0.2.

An important feature of the generated response functions, especially in channels 94 Å, 131 Å, and 193 Å is their bimodal temperature sensitivity. This is clearly visible in Figure 2.3. In the 94 Å channel, for example, AIA cannot distinguish between emission that is coming from plasma at $\log_{10}(T) = 6.0$ and $\log_{10}(T) = 6.9$. Additionally, AIA as a whole is not particularly sensitive to extremely high temperatures ($\gtrsim 10^7$ K).

2.2 DEM Inversion

Using the narrow-band images from AIA, we can determine the distribution of plasma temperatures along line-of-sight through a process known as **differential emission measure (DEM) inversion**.

2.2.1 Differential Emission Measure

Since emission from isothermal plasma is primarily due to free-free collisional radiation, it is therefore dependent upon the number densities of protons and electrons (assumed to be roughly equal in the solar atmosphere). In analyzing emission from the Sun, it then becomes useful to define a quantity known as the **(column) emission measure** (EM),

$$EM = \int n_e^2 dz, \quad (2.2.1)$$

which has units of cm^{-5} . Recasting this integral over temperature gives

$$EM = \int n_e^2 \frac{dz}{dT} dT \quad (2.2.2)$$

$$= \int DEM(T) dT \quad (2.2.3)$$

where

$$DEM(T) dT = n_e^2 dz \quad (2.2.4)$$

is the differential emission measure along the line-of-sight z , or **(column) differential emission measure**² (DEM), in units of $[\text{cm}^{-5}\text{K}^{-1}]$. The differential emission measure $DEM(T)$ is a function that describes the amount of emitting plasma at any given temperature, and it is used in solar physics to help characterize the distribution of plasma temperatures in the solar atmosphere [16, section 3.7].

Since temperatures of plasma in the corona can vary widely, it is convenient to use $\log(T)$ space to describe plasma temperature distributions. We have that

$$d(\log_{10} T) = \frac{1}{\ln(10)} \frac{dT}{T} \quad (2.2.5)$$

$$dT = \ln(10) T d(\log_{10} T) \quad (2.2.6)$$

so in log space, equation 2.2.3 becomes (ignoring the constant $\ln(10)$ which results from this transformation)

$$EM = \int T DEM(T) d(\log_{10} T). \quad (2.2.7)$$

² Note there is a distinction between column DEMs and volume DEMs, which is frequently left unspecified in literature. They can be converted to one another by taking into account the area of a given pixel; see [15, pp.41].

2.2.2 DEM Inversion

For any given pixel of an image taken in narrow wavelength band i , the following equation, given by [17], applies at any instant in time:

$$y_i = \int_0^\infty K_i(T) DEM(T) dT \quad (2.2.8)$$

where y_i is the measured brightness of the pixel [DN px $^{-1}$], $K_i(T)$ is the temperature response function [DN cm 5 px $^{-1}$], and $DEM(T)$ is the column differential emission measure [cm $^{-5}$ K $^{-1}$].

As before, we note that using logarithmic temperature is convenient, so we transform 2.2.8 to

$$y_i = \int_1^\infty K_i(T) T DEM(T) d(\log_{10} T) \quad (2.2.9)$$

producing y_i in units of [DN px $^{-1}$]. (Note that the integral is now dimensionless.³)

DEM inversion refers to inverting the integral in (2.2.8) or (2.2.9) to solve for $DEM(T)$. The problem is mathematically ill-posed; methods to solve for the DEM do not (and can not) always converge on a sensible solution [17]. However, in many cases, reasonable solutions may be determined, and several implementations of DEM inversion exist, which use various algorithms to invert AIA data. Each of these programs has its own merits and limitations, but invariably, all of them output a plausible solution for the EM or DEM that reproduces the observed intensities in all inputted AIA channels. These outputs may not completely match one another—since AIA channels are not spectrally pure and AIA channels exhibit a response to broad temperature ranges, many plausible DEM solutions generally exist—but are typically all similar. For this project, we chose to use the implementation distributed by the AIA team, presented in a paper by M. Cheung [17].

2.2.3 Sparse DEM Inversion

The implementation presented by [17], distributed in SolarSoft as the utility code `aia_sparse_em_init.pro`, first divides the logarithmic temperature range into n bins, converting the equation 2.2.9 into

$$y_i = \sum_{j=1}^n \int_{\log T_j}^{\log T_j + \Delta \log T_j} K_{ij} T DEM(T) d(\log_{10} T) \quad (2.2.10)$$

where the j th temperature bin has temperatures which range from $\log_{10} T_j$ to $\log_{10} T_j + \Delta \log_{10} T_j$. Then, it assumes that the function K_{ij} is piecewise constant

³ To justify taking the logarithm of an apparently dimensioned value T , see [18, pp. 68]; the chain rule allows this shorthand to be equivalent to $d(\log_{10}(T/K))$.

in each temperature bin j , allowing the problem to be formulated as a matrix equation

$$y_i = \sum_{j=1}^n K_{ij} EM_j \quad (2.2.11)$$

where EM_j is the emission measure as written in 2.2.7, over a specific temperature bin j :

$$EM_j = \int_{\log T_j}^{\log T_j + \Delta \log T_j} T \text{DEM}(T) d(\log_{10} T). \quad (2.2.12)$$

The implementation then minimizes the L1 norm of the vector \mathbf{y} for this equation by assuming the matrix is sparse, using a “simplex” method of optimization, and ensuring that solutions are positive. By default and in our usage, the program uses three Gaussians of various widths as basis functions for these matrices, with sigma values of 0.1, 0.2, and 0.6.

This approach is well-validated for AIA data, and this implementation has a significant advantage when compared to others: when it fails to produce a solution, it provides an informative error code. This prevents the program from running indefinitely, and prevents it from producing results beyond a certain uncertainty threshold.

An example of the type of output that this program produces for each pixel can be seen in Figure 2.4. For every pixel, the program outputs the emission measure EM in each temperature bin j , producing a function that describes the amount of the emission that comes from plasma of that temperature, along line-of-sight.

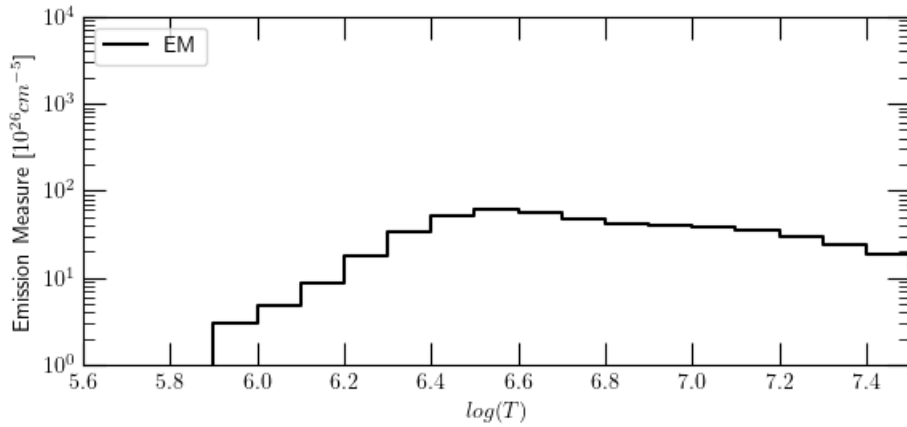


Figure 2.4: Example of EM curve outputted by the EM solver presented by [17].

Chapter 3

Data

3.1 Data Collection

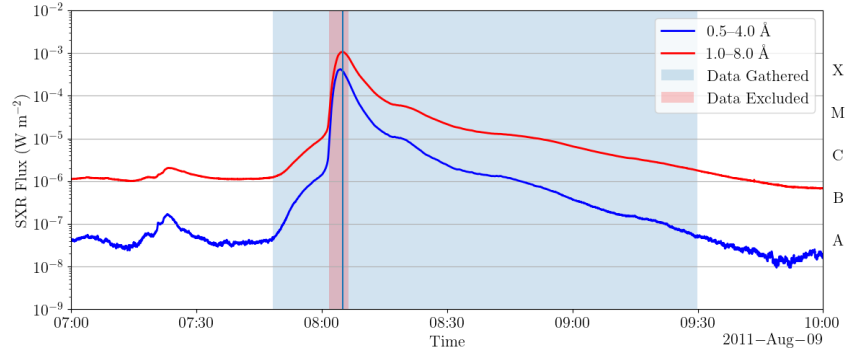
Using the Joint Science Operations Center (JSOC) database, we retrieved data for two long-duration X-class solar flares, whose soft X-ray (SXR) light curves (fluxes over time, as measured by GOES) can be seen in Figure 3.1. As is standard in studying solar flares, we used images from the six AIA channels mentioned in Section 2.1.3 that are sensitive to coronal, optically-thin plasma: 94, 131, 171, 193, 211, and 335 Å.

The first flare was an X6.9-class flare on the west solar limb that occurred on August 9, 2011, in the active region NOAA 11263. We obtained data spanning from 07:48 to 09:29 UTC. For this event, the soft X-ray (SXR) flux began to rise sharply at roughly 07:48 UTC (corresponding to the flare's impulsive phase) and peaked at 08:05 UT, then decayed for about 40 minutes (corresponding to the post-flare's gradual phase).

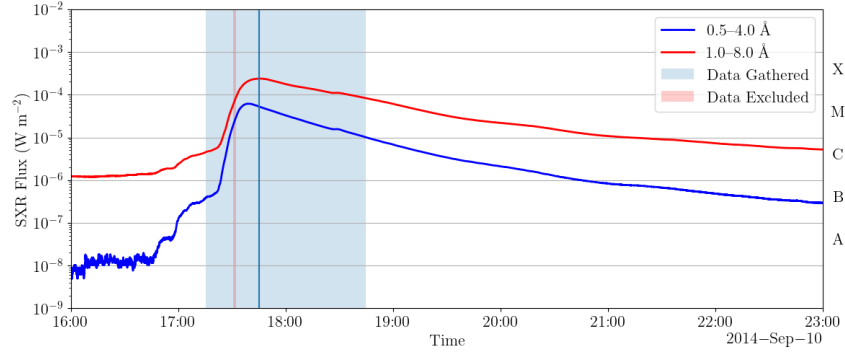
The second flare we studied was an X1.6-class flare that occurred on September 10, 2014, in the active region NOAA 12158, close to the center of the solar disk. We gathered data from 17:15 to 18:44 UTC. The SXR rise began at 17:21 UTC and peaked at roughly 07:45 UTC, followed by a decay lasting over 5 hours.

3.2 Data Processing

Due to AIA's automatic exposure control operation, image exposure time varies throughout the dataset. For each minute, we found the channel which had the lowest exposure time, and then found low-exposure images in other channels within the surrounding 24 sec and temporally aligned all of them together. This gave us images with the fewest possible saturated pixels and a temporal resolution of roughly 24 sec. As a consequence, our dataset contained roughly 100 time frames for both flares.



(a) Flare in AR 11263



(b) Flare in AR 12158

Figure 3.1: Geostationary Operational Environmental Satellite (GOES-15) X-ray light curves for the two flares considered in our study. The regions highlighted in blue represent the time ranges of observation for our study. The regions highlighted in red represent the data we did not consider, since the images were highly contaminated by diffraction. The red line represents X-rays in the 1–8 Å (long wavelength) band. The blue line represents X-rays in the 0.5–4 Å (short wavelength) range. The long wavelength band is used to classify solar flares. (a) X-ray light curve for the 2011 flare. (b) X-ray light curve for the 2014 flare. The left axes show soft X-ray (SXR) flux in W m^{-2} ; the right axes show flare classification levels, as defined in Table 1.1.

We processed the images into so-called Level 1.5 data using `aia_prep.pro` code from SolarSoftware. This program co-aligns, rescales, and rotates the image data to align with solar north, interpolating the images to the plate scale of $0.6''/\text{px}$ (a Nyquist resolution of $1.2''$). This process allows the images to be usable for further analysis, as the same pixels now represent the same locations on the Sun's disk.

We made a note of which pixels were saturated, and in how many channels. Next, we noted that even with no incoming photons, CCDs (by virtue of being electronics) may report a nonzero value for pixel intensity; this effect is called "dark current" and must be subtracted during analysis. We averaged expected dark current values over each quadrant of the images, and subtracted them from the processed images.

In order to minimize the effects of diffraction in each image, we then performed point-spread function (PSF) deconvolution using the Richardson-Lucy algorithm on each image. Figures 3.2 and 3.3 show samples of the AIA data after processing.

Even after these steps, some frames during the peaks of the flare were contaminated by diffraction. Out of an abundance of caution, we chose not to analyze data taken at these times: 08:01–08:06 for the flare in 2011; 17:30–17:32 for the flare in 2014. These temporal regions are highlighted in red in Figure 3.1.

After the initial processing of the data as described above, we ran the sparse DEM inversion method described in 2.2 with its standard settings to produce DEM curves for each inherent $0.6''$ AIA pixel, in every time frame, in temperature bins between $\log(T/\text{K}) = 5.6$ and $\log(T/\text{K}) = 7.5$, with $d(\log_{10} T) = 0.1$.

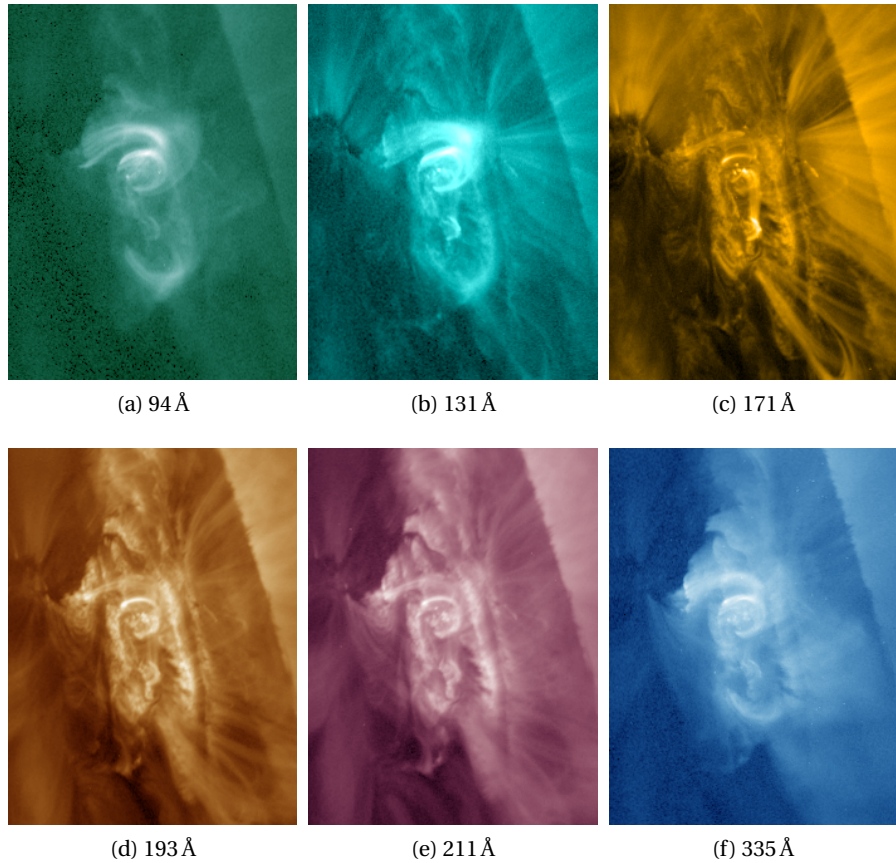
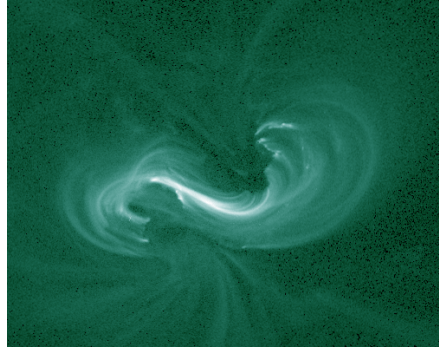
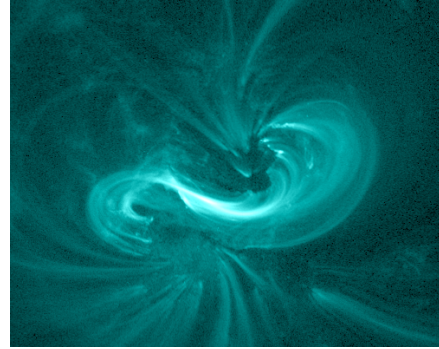


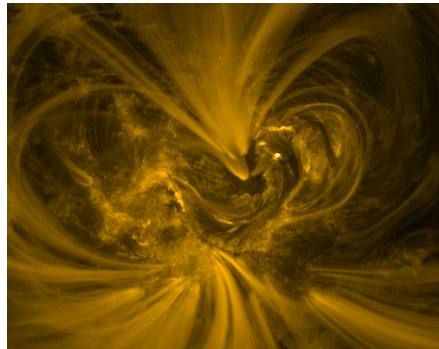
Figure 3.2: AR 11263 at 07:48, in six different wavelengths corresponding to optically thin plasma.



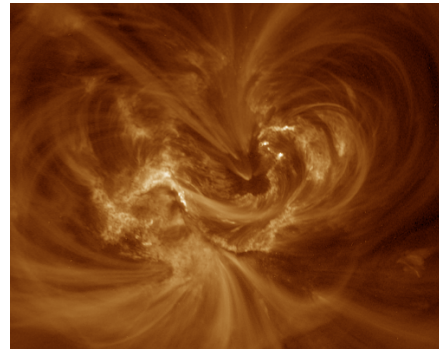
(a) 94 Å



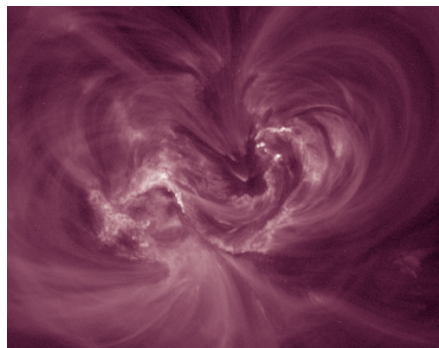
(b) 131 Å



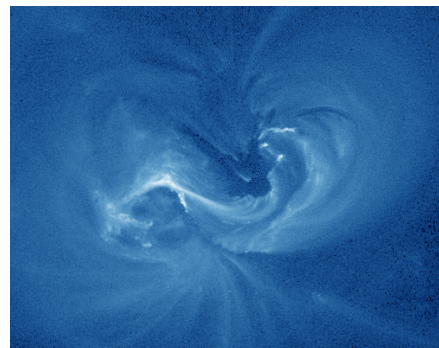
(c) 171 Å



(d) 193 Å



(e) 211 Å



(f) 335 Å

Figure 3.3: AR 12158 at 17:15, in six different wavelengths corresponding to optically thin plasma.

Chapter 4

Analysis of Inversion Failures

When we performed DEM analysis on our observations, we found that DEM inversion fails for certain pixels during our observations. More precisely, we discovered that failed pixels occur at the tops of flare loops, following the peak of the flare. A failed pixel produces no EM solution like the one in Figure 2.4.

Visually, we can see this in the images like in Figure 4.1, where the color scale is the cumulative emission measure (the total output of the solver, summed over temperature). In these images, pixels where DEM inversion failed are shown as black.

The fact that these failures are highly localized is intriguing, and motivated our investigation into the potential causes.

4.1 Saturation

Flares produce bright emission throughout their evolution. Due to this, a few saturated pixels still exist in the images even after processing them, so our first hypothesis was that the DEM failures were due to poor data quality due to pixel saturation. We produced plots of the cumulative emission measure, with contoured regions showing where pixels were saturated. A sample of these images is shown in Figure 4.1.

We found that the pixels that were saturated did not always overlap with the failed DEM pixels. This is especially obvious in the 2014 flare, where very few pixels were saturated throughout a majority of the data set. We concluded that saturation could not be the primary reason that DEM failures occurred.

4.2 Status Codes

As was briefly described in Section 2.2.3, the implementation of DEM inversion as presented by [17] provides error codes when the algorithm fails to produce a

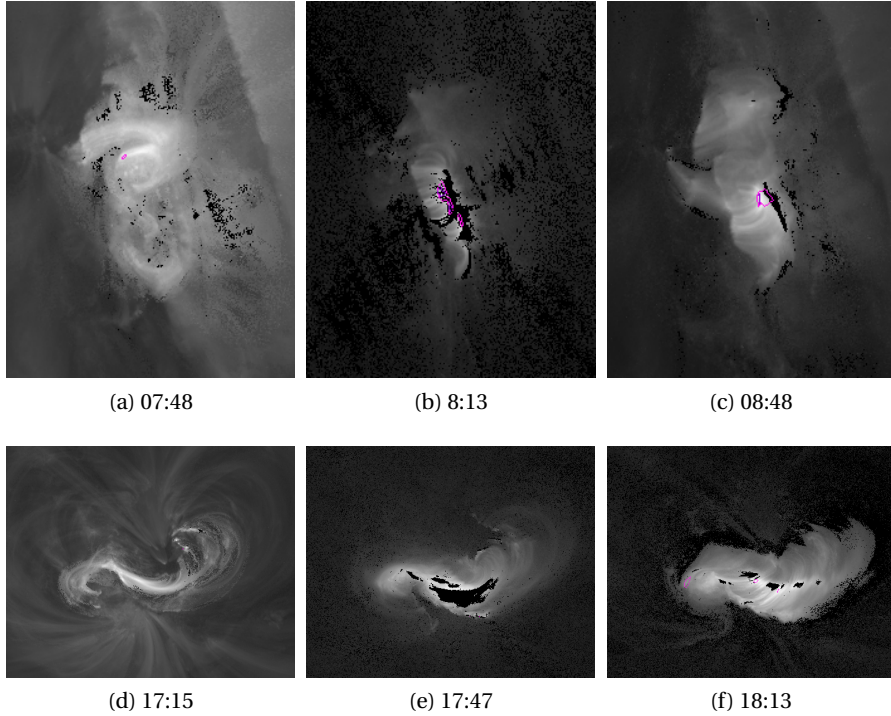


Figure 4.1: The cumulative emission measure summed over temperature [cm^{-5}] shown in grayscale at three different timesteps: pre-flare (panels a and d), slightly after flare peak (panels b and e), and post-flare (panels c and f). The top row shows the 2011 flare; the bottom row shows the 2014 flare. Pink contours outline regions where at least one channel of data is saturated (DN greater than 15000); purple indicates three or more channels. DEM inversion methods continue to fail in the post-flare stages in areas with no saturation. The images chosen are for demonstrative purposes; for typical frames, less saturation is typically present.

solution. This provides us with a starting point to learn about potential reasons the program fails.

The implementation of DEM inversion relies on the simplex algorithm, a linear programming method based on iterative optimization of a so-called ‘objective function’ (which in this case, effectively means minimizing the L1 norm of the emission measure function). This means that the following errors are possible:

1. The objective function is unbounded (the problem has no *optimal* solution),
2. No solution satisfies the given constraints (the problem has *no* solution),

3. The routine did not converge (could mean the routine cycled or stalled)
4. The routine mistakenly did not give a positive solution despite the constraints (implementation error).

In examining the resulting error codes, we found that error 3 was present at the edges of the flare, as shown in Figure 4.2 in a light green color. This is not surprising as the data in these regions may be of poor quality: since the exposure time is so short, the regions with less emission have a low ratio of signal-to-noise, as compared to data at the center of the image. In contrast, error 2 consistently appeared during the peak of the flare (during the times of high diffraction that we discarded as mentioned in Section 3.2). This error also appeared after the peak of the flare at the tops of flare loops. In other words, the problem had no solutions for spatial regions where data was of poor quality, *and* after the peaks of flares at the tops of the flare loops, regardless of the data quality.

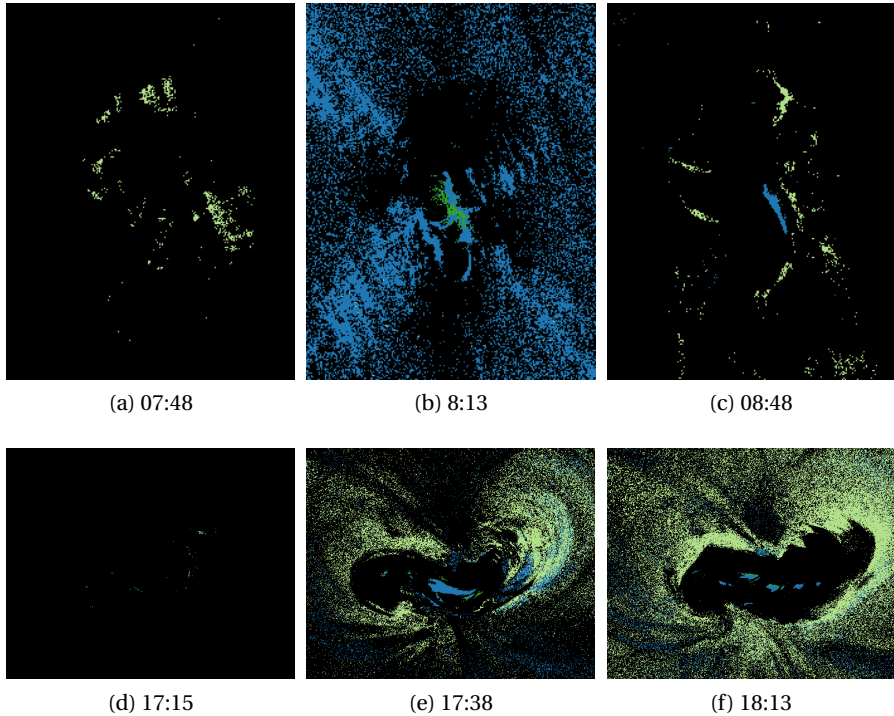


Figure 4.2: Status code outputs of [17] DEM inversion program at three timesteps: pre-flare, slightly after flare peak, and post-flare. Light green pixels indicate where the method failed to converge, implying solutions are poorly constrained or the implementation itself failed; these pixels occur at most frames in any analysis and are considered to be artifacts or noise. Blue pixels indicate where no solution exists; i.e., no thermal distribution can possibly account for the observed emission.

4.3 Spatial Locations

To investigate this phenomenon further, we considered our images in the context of a standard model of a solar flare, as shown in Figure 4.3. While solar flares are all unique, they all are based in the phenomenon of magnetic reconnection, and many have visible loops that extend out of the surface of the Sun. We consistently see that DEM inversion failures occur at the tops of flare loops — right at the locations where magnetic reconnection is theorized to occur. This is especially visible in, e.g., Figures 4.1c and 4.1f.

With this in mind, we have turned our attention to other data sets. How is it possible that other studies, e.g., [19], have seemingly been able to determine DEM solutions of solar flares? The answer is that, throughout the literature, solar physicists degrade the resolution of AIA data, averaging nearby pixels together. This smooths out anomalies and results in DEM solutions in nearly every pixel for an image.

Additionally, some studies involve other instruments that are sensitive to higher temperatures, e.g., the X-Ray Telescope (XRT) on the Hinode telescope. This can improve convergence. But data from these instruments also has poorer resolution, both spatially and temporally. Combining AIA data with these instruments is challenging, and inevitably requires rebinning images to a degraded resolution.

It seems, then, that DEM solutions can only be derived when AIA images are analyzed with degraded resolution. However, this is far from a satisfying result, and does not answer the underlying question of *why* DEM inversions fail during solar flares. AIA data is valuable precisely because it allows us to examine the finer structures in the solar atmosphere over short timescales. DEM inversion failures are evidently highly spatially localized.

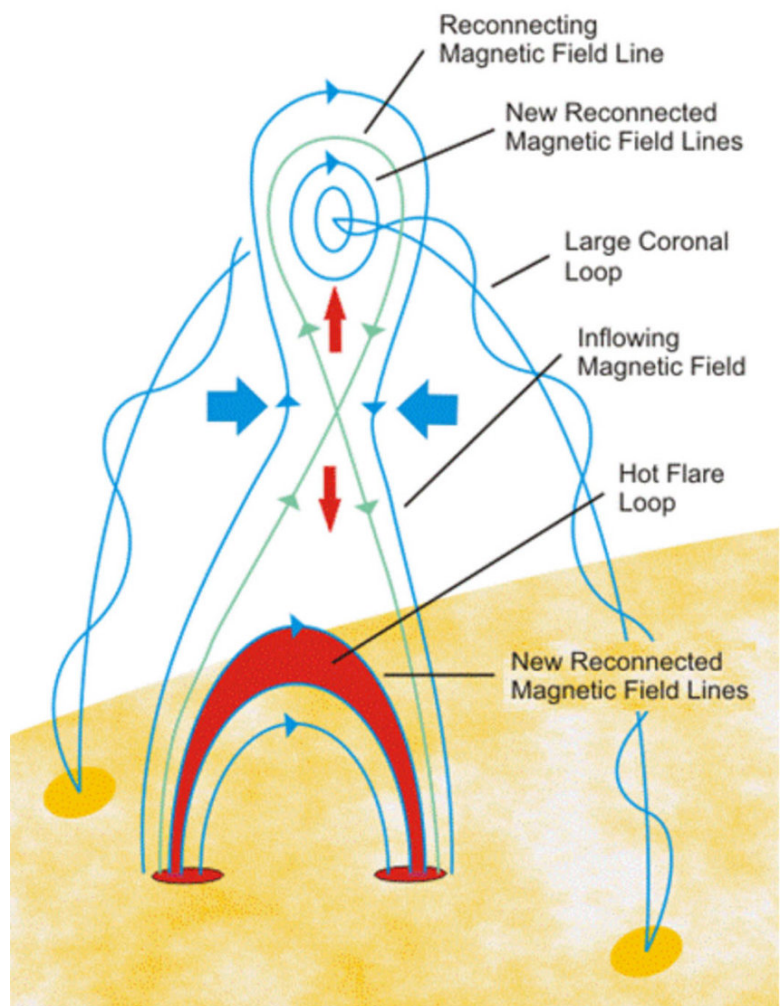


Figure 4.3: Standard model of a solar flare, from [20]

4.4 Loci Plots

We wanted to see if there were other anomalous features of the data in failed pixels.

Recall that the DEM inversion implementation relies upon equation 2.2.11:

$$y_i = \sum_{j=1}^n K_{ij} EM_j. \quad (4.4.1)$$

This equation assumes that the thermal response function K of the instrument in channel i and temperature j is roughly piecewise constant over a temperature bin j . It implies that the intensity measured in channel i is due to the portion of emission in a temperature bin j , combined with the instrument's thermal response function value in temperature bin j .

For an *isothermal* plasma, i.e., plasma which has a single temperature T , the equation is instead simply

$$y_i = K_i(T) EM(T) \quad (4.4.2)$$

which means that the emission measure can be given by

$$EM(T) = \frac{y_i}{K_i(T)}. \quad (4.4.3)$$

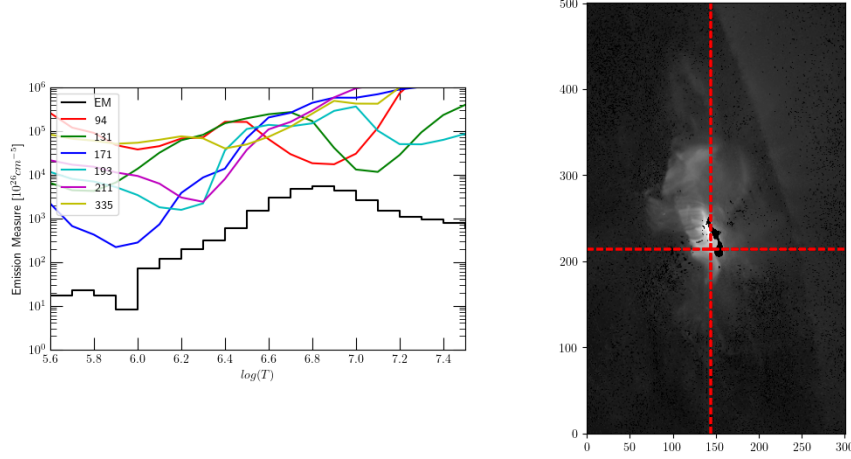
In theory, given observational data of an isothermal plasma, if we were to plot $EM(T)$ for each channel, then all of the functions would cross at a single point, corresponding to the temperature of the plasma and its emission measure.

In practice, plasma is not isothermal. For a *multithermal* plasma, the emission measure will be the sum of emission measures due to plasma at multiple temperatures, so the value found by equation (4.4.3) must provide an upper bound for the amount of emission measure from any given temperature [16, see chapter 7] [1, 21].

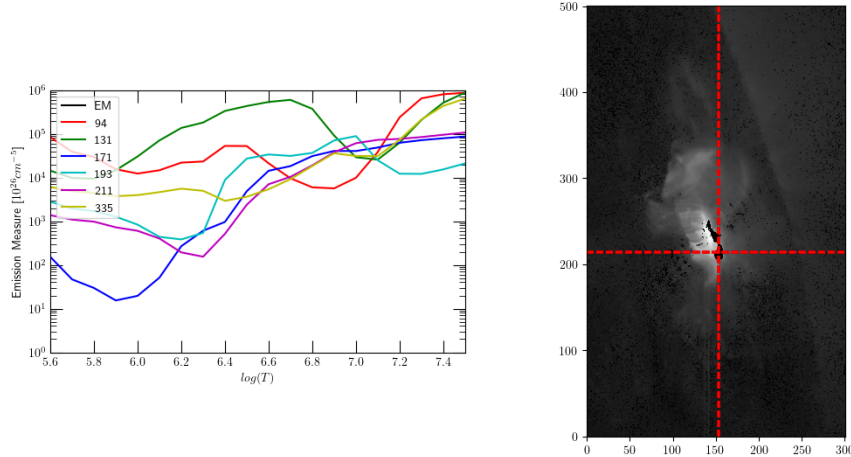
To verify our DEM solutions for any given pixel, we can plot these upper bounds as defined by 4.4.3 for each channel and compare them to the calculated EM curves, to ensure that our results make sense. An example result can be seen in Figure 4.4a. This method is known as the loci method.

We developed a program to visually compare loci curves temporally and spatially. A potential result is that, during the post-flare phase on the top of the flare loop, it appears that certain channels associated with high temperatures (e.g., 94 Å, 131 Å) appear to "lift" — the emission in these channels is higher than in other channels. This can be seen in Figure 4.4b.

The main reason that this may cause the DEM inversion method to fail is the shape of the response curves. As mentioned in 2.1.3, AIA is not particularly sensitive to high temperatures; additionally, some AIA channels are bimodal in their sensitivity. This means that if these bimodal channels are receiving strong



(a)



(b)

Figure 4.4: On the left are EM loci curves for two different locations at the same time, calculated using equation 4.4.3 for each channel (as labeled in the legend). On the right is displayed the cumulative emission measure for each pixel in the flare, as in 4.1. **Top:** The DEM solution (black line on left plot) exists. **Bottom:** There is no DEM solution. We note that the loci curves (colored lines) for certain channels are “lifted”, i.e., we see more emission in these channels than in others.

emission from high-temperature plasma, DEM inversion methods cannot find a solution that satisfies all constraints.

The temperature response curves combine optical qualities of the observing telescopes with the physical properties assumed for the observed plasma. Typi-

cally, these assumptions include that the emitting plasma is in thermal and ionization equilibrium. These parameters work well on the quiet Sun. However, solar flares release immense amounts of energy and involve strong magnetic fields; it is feasible that non-equilibrium ionization states may be present. In this case, the equilibrium assumptions could exclude viable temperature distributions. It may be that no plasma in equilibrium could emit the observed intensities, and therefore, no solution could be found.

Another assumption is that the plasma has coronal abundances. However, flares can bring material from the photosphere into the corona; this may affect the types of emission measured.

Finally, DEM inversion assumes that coronal plasma is optically thin. However, flares can have higher density than the surrounding solar atmosphere; this may fundamentally change the nature of emission measured from solar flares.

4.5 Conclusions and Further Study

The discovery that DEM inversions consistently fail at the tops of X-class flare loops, but that the nearby solutions appear to be reasonable, implies that the source of the problem is less likely to be an artifact of the data, and more likely to be due to the emitting plasma itself at these locations.

Several avenues of study are open for investigation. In continuing this work, we are looking to do DEM inversion on a larger data set of flares. We have selected 18 additional flares ranging from M1.1 to X1.1, and are currently running DEM inversion processes on each flare. We hope to study if DEM inversion failures occur for M-class flares as well as X-class flares. This would demonstrate strong evidence that solar flares share specific characteristics regardless of their size. We are also investigating non-equilibrium thermal response curves and adjusting coronal abundances, to change the shape of the response curves and test if this improves convergence.

Bibliography

- [1] K. J. H. Phillips, U. Feldman, and E. Landi, *Ultraviolet and X-ray Spectroscopy of the Solar Atmosphere*, ser. Cambridge Astrophysics. Cambridge University Press, 2008. (cited on page 4, 8, 13, 30)
- [2] ScienceFacts.net, “Layers of the sun.” [Online]. Available: <https://www.sciencefacts.net/layers-of-the-sun.html> (cited on page 5)
- [3] M. Druckmüller, “Solar corona during 19 s long total solar eclipse.” [Online]. Available: http://www.zam.fme.vutbr.cz/~druck/Eclipse/Ecl2013u/Tse_2013_hsd/0-info.htm (cited on page 5)
- [4] M. B. Larson, “Temperature vs. radius in the solar atmosphere,” adapted from Sun, Earth, Sky by Kenneth Lang. [Online]. Available: <https://solar.physics.montana.edu/ypop/Spotlight/SunInfo/transreg.html> (cited on page 6)
- [5] S. Toriumi and H. Wang, “Flare-productive active regions,” *Living Reviews in Solar Physics*, vol. 16, no. 1, p. 3, May 2019. doi: 10.1007/s41116-019-0019-7 (cited on page 7)
- [6] S. R. Kane, *Impulsive (Flash) Phase of Solar Flares: Hard X-Ray, Microwave, EUV and Optical Observations*. Dordrecht: Springer Netherlands, 1974, pp. 105–141. ISBN 978-94-010-2257-6 (cited on page 9)
- [7] LMSAL. [Online]. Available: https://suntoday.lmsal.com/suntoday/?suntoday_date=2024-04-25 (cited on page 12)
- [8] J. R. Lemen, A. M. Title *et al.*, “The atmospheric imaging assembly (AIA) on the solar dynamics observatory (SDO),” *Solar Physics*, vol. 275, no. 1–2, p. 17–40, Jun. 2011. doi: 10.1007/s11207-011-9776-8 (cited on page 11, 13)
- [9] M. J. Aschwanden, “The spatio-temporal evolution of solar flares observed with AIA/SDO: Fractal diffusion, sub-diffusion, or logistic growth?” *The Astrophysical Journal*, vol. 757, no. 1, p. 94, Sep. 2012. doi: 10.1088/0004-637X/757/1/94. [Online]. Available: <http://dx.doi.org/10.1088/0004-637X/757/1/94> (cited on page 11)

- [10] R. W. Nightingale, “AIA/SDO FITS keywords for scientific usage and data processing at levels 0, 1.0, and 1.5,” Lockheed-Martin Solar and Astrophysics Laboratory (LMSAL), Tech. Rep. AIA02840, March 2011. [Online]. Available: http://jsoc.stanford.edu/~jsoc/keywords/AIA/AIA02840_N_AIA-SDO_FITS_Keyword_Document.pdf (cited on page 13)
- [11] B. O’Dwyer, G. Del Zanna *et al.*, “SDO/AIA response to coronal hole, quiet Sun, active region, and flare plasma,” *Astronomy & Astrophysics*, vol. 521, p. A21, Oct. 2010. doi: 10.1051/0004-6361/201014872 (cited on page 13)
- [12] P. Boerner, C. Edwards *et al.*, “Initial calibration of the atmospheric imaging assembly (AIA) on the solar dynamics observatory (SDO),” *Sol. Phys.*, vol. 275, no. 1-2, pp. 41–66, Jan. 2012. doi: 10.1007/s11207-011-9804-8 (cited on page 13, 14)
- [13] G. Del Zanna, K. P. Dere *et al.*, “CHIANTI—An atomic database for emission lines. XVI. version 10, further extensions,” *The Astrophysical Journal*, vol. 909, no. 1, p. 38, Mar. 2021. doi: 10.3847/1538-4357/abd8ce (cited on page 15)
- [14] U. Feldman, P. Mandelbaum *et al.*, “The potential for plasma diagnostics from stellar extreme-ultraviolet observations,” *The Astrophysical Journal Supplement*, vol. 81, pp. 387–408, Jul. 1992. doi: 10.1086/191698 (cited on page 15)
- [15] G. Del Zanna, *CHIANTI: An Atomic Database for Astrophysical Plasmas*, 2019. [Online]. Available: <https://www.chiantidatabase.org/cug.pdf> (cited on page 16)
- [16] G. Del Zanna and H. E. Mason, “Solar UV and X-ray spectral diagnostics,” *Living Reviews in Solar Physics*, vol. 15, no. 1, p. 5, Aug. 2018. doi: 10.1007/s41116-018-0015-3 (cited on page 16, 30)
- [17] M. C. M. Cheung, P. Boerner *et al.*, “Thermal diagnostics with the atmospheric imaging assembly on board the solar dynamics observatory: A validated method for differential emission measure inversions,” *The Astrophysical Journal*, vol. 807, no. 2, p. 143, Jul. 2015. doi: 10.1088/0004-637x/807/2/143 (cited on page 17, 18, 24, 27)
- [18] C. F. Matta, L. Massa *et al.*, “Can one take the logarithm or the sine of a dimensioned quantity or a unit? dimensional analysis involving transcendental functions,” *J. Chem. Educ.*, vol. 88, no. 1, pp. 67–70, Jan. 2011. doi: 10.1021/ed1000476 (cited on page 17)
- [19] J. Q. Sun, X. Cheng, and M. D. Ding, “Differential emission measure analysis of a limb solar flare on 2012 July 19,” *The Astrophysical Journal*, vol. 786, no. 1, p. 73, apr 2014. doi: 10.1088/0004-637X/786/1/73 (cited on page 28)

- [20] G. Holman, adapted from the original image from Shibata (1996). [Online]. Available: <https://smallsat.umn.edu/about/solar-flares> (cited on page 29)
- [21] J. T. Schmelz, B. S. Jenkins *et al.*, “Isothermal and multithermal analysis of coronal loops observed with AIA,” *The Astrophysical Journal*, vol. 731, no. 1, p. 49, Apr. 2011. doi: 10.1088/0004-637X/731/1/49 (cited on page 30)